PAN

Opto-Electronics Review

journal homepage: https://journals.pan.pl/opelre

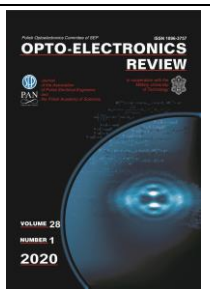


# Status of multi-wafer production MBE capabilities for extended SWIR III-V epi materials for IR detection

Everett D. Fraser*, Jiayi Shao, Paul W. Frensley, Beau D. Barnes, Kevin P. Clark, Yung-Chung Kao, Paul R. Pinsukanjana

Intelligent Epitaxy Technology, Inc. 1250 E. Collins Blvd., Richardson, TX 75081, USA

**Article info**

*Article history:*
Received 30 Nov. 2022
Received in revised form 09 Jan. 2023
Accepted 14 Jan. 2023
Available on-line 24 Feb. 2023

*Keywords*:
Extended shortwave; GaSb; InP; detector; pn-CBIRD.

**Abstract**

The authors report two approaches, the first based on growth of lattice matched InGaAs/GaAsSb superlattice on InP substrate with tunable bandgap in the 2 to 3 μm range. The second approach is based on bulk random alloy InGaAsSb, which is tunable from 1.7 μm to 4.5 μm and lattice matched to the GaSb lattice constant. In each case, detector structures were fabricated and characterised. The authors have assessed the performance of these materials relative to commercially available extended short wave infrared devices through comparison to IGA-Rule 17 dark current performance level. A complementary barrier structure used in the InGaAsSb design showed improved quantum efficiency. The materials compare favourably to commercial technology and present additional options to address the challenging extended short wave infrared spectral band.

## 1. Introduction

The infrared spectral band spanning from 1 to 3 μm is of interest for various commercial and military applications. This extended short wave infrared (SWIR) wavelength range offers key fingerprints of various chemical, biological, and explosive materials [1]. Commercial applications include agricultural crop inspection [2] and plastics recycling [3]. Wearable consumer products which track user bioinformation and health indicators, which have signatures in the extended SWIR wavelength range [4], are gaining traction in recent years. Semiconductor materials with bandgap sufficient to address the infrared spectral wavelength band from 1 to 3 μm have traditionally been a challenge for detector applications. For example, the band can be accessed via either HgCdTe [5] or high indium mole fraction InGaAs on InP substrate [6]. HgCdTe can suffer from weak bond strength and difficult control of mole fraction, both of which can lead to non-uniformity within detector array. HgCdTe detectors tend to rely on CdZnTe substrate which are not US domestic products and are difficult to manufacture with large area. Extended InGaAs detection is hindered by defects introduced due to the lattice mismatch between the active layers and the InP substrate. The threading dislocations resulting from the mismatched deposition give rise to high levels of dark current, impacting detector performance.

Several III-V-based approaches have been demonstrated to address the extended SWIR band [7, 8] and provide potential solutions which could exploit the manufacturability and uniformity advantages of molecular beam epitaxy (MBE) volume manufacturing. In this report, the authors present results on two III-V approaches for extended SWIR detection, both of which result in lattice matched material to commercially available III-V substrates and produced on multi-wafer production systems. The first approach is based on the InP lattice constant and employs a type II superlattice of InGaAs and GaAsSb, both layers lattice matched to the substrate. The spatially indirect transition from the InGaAs conduction band to the GaAsSb valence band allows for sensitivity to cut-off wavelengths within the 1 to 3 μm spectral range, with wavelength control through adjustment of the superlattice period. The advantage of the InP approach is that it allows for development based on the established InGaAs processing and manufacturing infrastructure, including the option to produce arrays with junctions

*Corresponding author at: efraser@intelliepi.com

https://doi.org/10.24425/opelre.2023.144571
1896-3757/ Association of Polish Electrical Engineers (SEP) and Polish Academic of Sciences (PAS). Published by PAS

defined via diffusion process. The disadvantage of the approach is reliance on the spatially indirect gap, limiting material absorption. On the other hand, InGaAsSb lattice matched to GaSb retains a direct gap, strong material absorption and can build on the existing GaSb-based type II strained layer superlattice focal plane array (SLS FPA) processing infrastructure. InGaAsSb can be conceptualised as a mixture of GaSb and lattice matched $InAs_{0.91}Sb_{0.09}$ and the degree of mixing controls the material bandgap from about 1.7 µm (GaSb) to near 4.5 µm (InAsSb). The InGaAsSb absorber has shown good performance in XBn barriode-based device architecture [9] for extended SWIR detection applications.

## 2. Experimental procedure

The extended SWIR materials were grown by a solid source MBE using a Riber MBE6000 multi-wafer production platform. The system is specifically equipped for growth of GaSb-based infrared products at production level volumes. Wafer capacity is 15×3 in, 9×4 in, 7×5 in, or 4×6 in. The system has 11 source ports and is equipped with valved cracking cells for the group V materials. Product types include materials for infrared FPA fabrication spanning the thermal bands from 2 µm to 15 µm and in both single-band and bias-selectable dual-band configurations. Additionally, the system is used to address environmental and industrial gas sensing application based on both inter-band cascade emitters and type II SLS detectors.

The extended SWIR materials were examined post growth, using Surfscan (SS) inspection, high-resolution X-ray diffraction (HRXRD), and Fourier transform infrared (FTIR) spectroscopy photoluminescence (PL) measurement at room temperature. Device diodes were processed using standard photolithography and wet chemical etching with a tartaric based solution to create 200 µm×200 µm square mesas. The processed test chips were bonded to 68 pin leadless chip carriers for measurement by variable temperature current-voltage and topside illuminated FTIR spectral response. The device external quantum efficiency (QE) is estimated based on normalization to reference detector of known QE and cut-off wavelength found, defined as the wavelength at which responsivity is 50% of maximum.

## 3. Results

### *3.1. InP-based approach*

The epitaxial layer structure for the InP-based InGaAs/GaAsSb approach is shown in Fig. 1. The device architecture is a PIN detector structure consisting of a semi-insulating InP substrate on which an initial 500 nm layer of lattice matched $In_{0.53}Ga_{0.47}As$ silicon doped to $2{\cdot}10^{18}$ $cm^{-3}$ was deposited. The absorber layer consists of 400 repeats of a 5nm/5nm lattice matched $In_{0.53}Ga_{0.47}As/GaAs_{0.5}Sb_{0.5}$ superlattice. The top contact is formed by 500 nm of $In_{0.53}Ga_{0.47}As$ doped with beryllium to $8{\cdot}10^{18}$ $cm^{-3}$. The compositions and layer thicknesses were verified using high-resolution X-ray diffraction (HRXRD) on the grown material and on separate calibration growths. The effective bandgap of the superlattice absorber and the PIN device band structure were calculated using an NRL Multiband simulation software suite [10]. The absorber bandgap was simulated as 2.34 µm at room temperature which is consistent with PL observed with peak wavelength of 2.38 µm. The simulated device band structure is shown in Fig. 2.

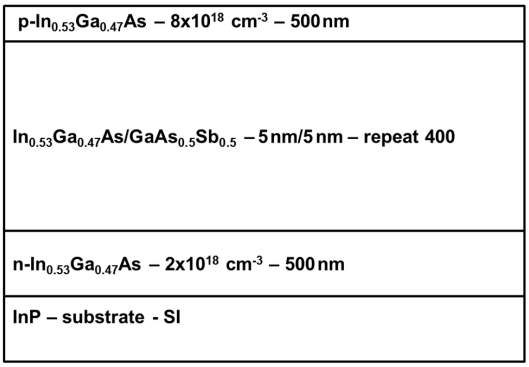


**Fig. 1.** The epilayer sequence of the InGaAs/GaAsSb PIN detector structure.

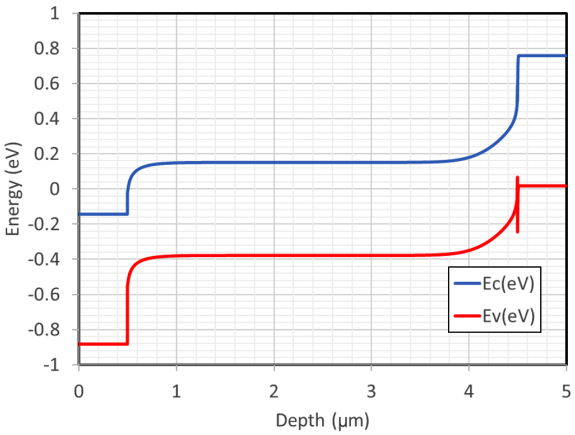


**Fig. 2.** The simulated band structure of the InGaAs/GaAsSb PIN detector structure.

As an initial characterisation of the multi-wafer deposition process, three GaSb wafers were loaded to the Riber MBE6000 platform positioned at the centre, inner ring and outer ring platen positions. By PL characterisation of the three wafers, a measure of the deposition uniformity of the entire deposition surface can be obtained. The PL intensity and peak wavelength position across the growth platen is shown in Fig. 3. The emission wavelength is uniform across the growth platen with only a 0.1 µm deviation from the platen centre, with a peak position of 2.58 µm, to the outermost edge, peak near 2.49 µm. The result is consistent with optimization of the production platform for material deposition uniformity and is an indication the material composition is reasonably uniform. PL intensity shows more variation at various platen locations, attributed to variations in growth conditions across the reactor and alignment during PL measurement.

Mesa diode structures were measured for current-voltage characteristics at various temperatures from 77 K to room temperature. In Fig. 4, the current-voltage measurements are shown. Figure 5 shows the Arrhenius plots of the dark current density taken at a bias of −50 mV. The activation energy down to about 200 K was found to be 0.28 eV, nearly $E_g/2$. The dark current behaviour characteristic of

the Shockley-Read-Hall (SRH) dark current or possibly surface recombination, as the dominant mechanism. The devices were processed by wet chemical etching and are un-passivated. The solid line in the plot is the indication of IGA Rule 17 [11], a heuristic metric for the dark current performance of commercially available detectors operating in the extended SWIR wavelength band. In Fig. 6, the dark current density dependence on the perimeter to the area ratio at 200 K, 250 K and 300 K, and a bias of −50 mV are presented. Only a weak dependence is observed, indicating that the current originates within the bulk materials as opposed to on the etched mesa surface.

The spectral QE is shown in Fig. 7. The cut-off wavelength is measured as near 2.3 µm at 200 K and red shifts to about 2.4 µm at 300 K. The QE magnitude is stable over the temperature range, with 10%~15% in the spectral range beyond 2 µm.

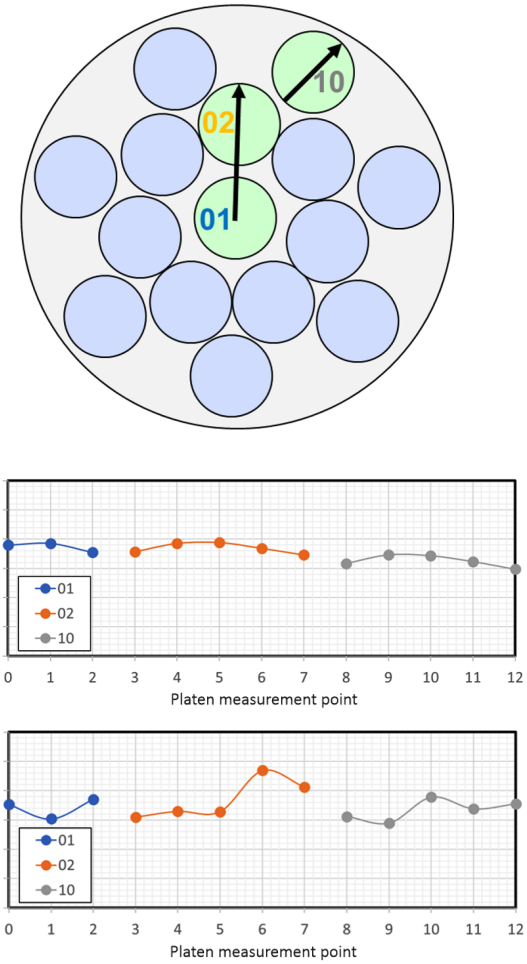


**Fig. 3.** Room temperature PL peak wavelength and intensity measured at different positions across the growth platen.

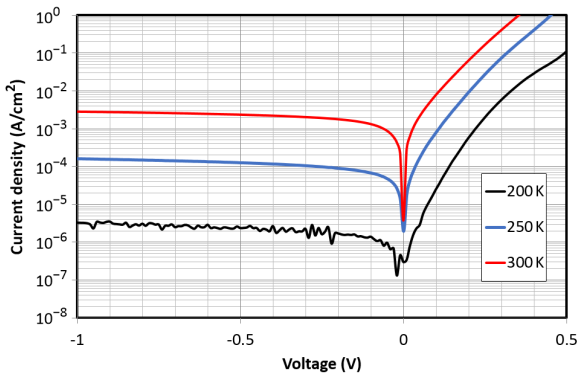


**Fig. 4.** Current-voltage measurement at various temperatures from 200 K to 300 K for the InP-based PIN extended SWIR detector.

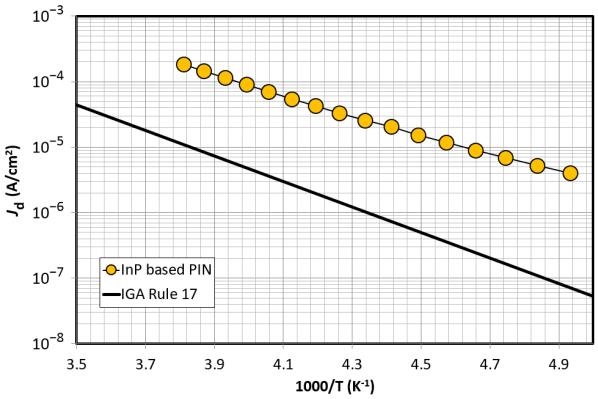


**Fig. 5.** Arrhenius plot of the dark current density measurement at various temperatures from 200 K to 300 K and −50 mV bias for the InP-based PIN extended SWIR detector.

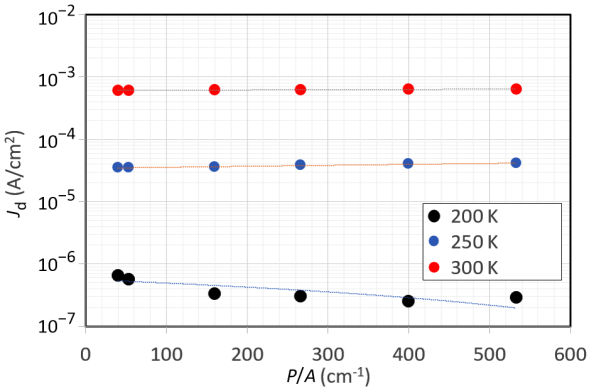


**Fig. 6.** Perimeter over area analysis of the PIN dark current density at 200 K, 250 K, and 300 K. Weak perimeter dependence is observed, indicating the dark currents originate within the bulk material.

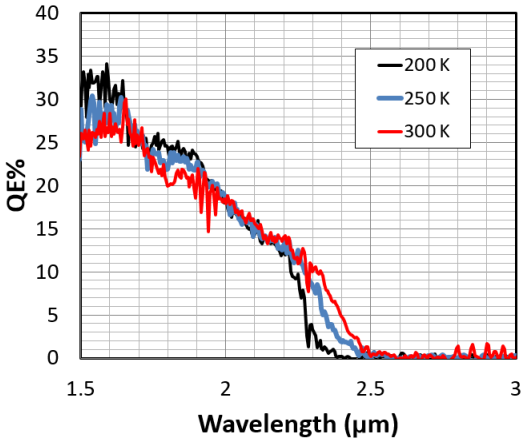


**Fig. 7.** QE at various temperatures from 200 K to 300 K for the InP-based PIN extended SWIR detector.

### 3.2. GaSb-based approach

The GaSb-based extended SWIR approach device architecture is based on the pn-complementary barrier infrared detector (pn-CBIRD) scheme developed by the infrared detector group at JPL [12, 13] which utilizes complimentary hole and electron barriers and sections of both n-type and p-type absorber material. The benefit of the device architecture is that the device has the advantages of both minimized etching depth, requiring mesa isolation only to the n-type section, and the longer diffusion length of the p-type absorbing material. The epitaxial layer structure for the GaSb-based InGaAsSb approach is shown in Fig. 8. The pn-CBIRD detector structure consists of an n-type GaSb substrate on which an initial 500 nm layer of lattice matched $In_{0.29}Ga_{0.71}As_{0.25}Sb_{0.75}$ tellurium-doped to $1{\cdot}10^{18}$ cm$^{-3}$ was deposited as a bottom n-type contact layer and hole barrier. The absorber layers consist of 2000 nm of n-type $In_{0.29}Ga_{0.71}As_{0.25}Sb_{0.75}$ and 2000 nm of p-type $In_{0.29}Ga_{0.71}As_{0.25}Sb_{0.75}$. The absorber layers are followed by an undoped layer of as an $Al_{0.22}Ga_{0.78}Sb$ 100 nm electron barrier, which will arrest parasitic dark currents, particularly on the device mesa surface layers. The top contact is formed by 100 nm of $In_{0.29}Ga_{0.71}As_{0.25}Sb_{0.75}$ doped with beryllium to $1{\cdot}10^{17}$ cm$^{-3}$. The compositions and deposition rates were verified using HRXRD on the grown material and on separate calibration growths. The effective bandgap of the absorber and the pn-CBIRD device band structure were calculated using the NRL Multiband simulation software suite. The simulated device band structure is shown in Fig. 9.

| |
|---|
| p-$In_{0.29}Ga_{0.71}As_{0.25}Sb_{0.75}$ – 1 × $10^{17}$ cm$^{-3}$ – 1000 nm |
| $Al_{0.22}Ga_{0.78}Sb$ – uid - 100 nm |
| p-$In_{0.29}Ga_{0.71}As_{0.25}Sb_{0.75}$ – 1 × $10^{16}$ cm$^{-3}$ – 2000 nm |
| n-$In_{0.29}Ga_{0.71}As_{0.25}Sb_{0.75}$ – 1 × $10^{16}$ cm$^{-3}$ – 2000 nm |
| n-$In_{0.29}Ga_{0.71}As_{0.25}Sb_{0.75}$ – 1 × $10^{18}$ cm$^{-3}$ – 500 nm |
| n-GaSb – substrate |

**Fig. 8.** The epilayer structure for the InGaAsSb pn-CBIRD detector structure.

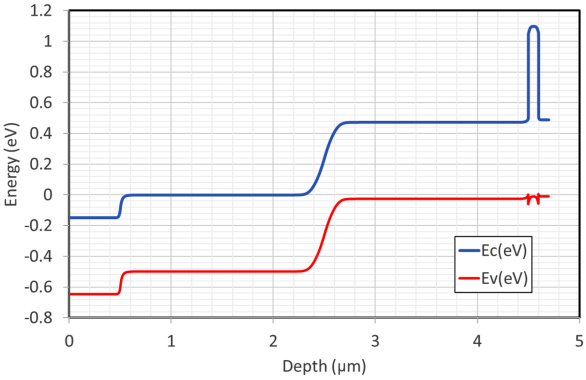


**Fig. 9.** The band-structure of the InGaAsSb pn-CBIRD detector structure calculated by NRL Multibands simulation suite.

From the pn-CBIRD device structure growth run, mesa diode structures were processed and measured for current-voltage characteristics at various temperatures. In Fig. 10 the current-voltage measurements are shown from 180 K to 300 K. Figure 11 shows the Arrhenius plots of the dark current density for the InGaAsSb-based detector measured at a bias of −50 mV. The activation energy down to about 180 K found to be 0.41 eV which, in contrast to the InP-based device presented, is close to $E_g$ behaviour and indicates diffusion current dominate the dark current process. The result is a good indication that complimentary barrier architecture is effective at suppressing the SRH and other parasitic dark current mechanisms. Included in the plot is the solid line showing the IGA Rule 17 metric. While the InP-based superlattice solution showed only a close approach to the Rule 17 values, the GaSb-based device does meet the Rule 17 criteria by room temperature operating condition. In Fig. 12, the authors present the dark current density dependence on the perimeter to the area ratio at 200 K, 250 K and 300 K, and a bias of −50 mV. As opposed to the results observed on the InP based structure, there is an apparent dependence on the P/A ratio indicating a surface current contribution to the dark current density which is not fully suppressed by the electron barrier layer. The result indicates a potential avenue for further performance improvement with device passivation.

The spectral QE is shown in Fig. 13. The cut-off wavelength is measured as near 2.6 μm at 200 K and red

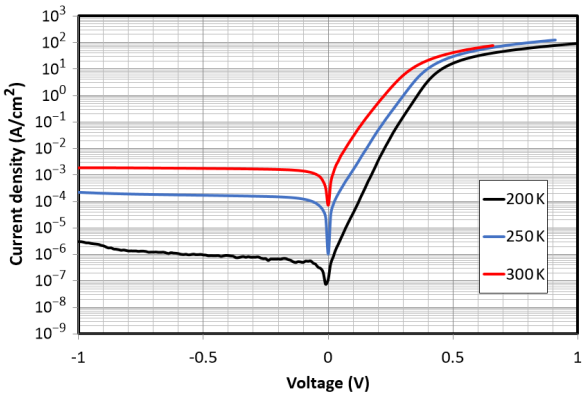


**Fig. 10.** Current-voltage measurement at various temperatures from 200 K to 300 K for the GaSb-based pn-CBIRD extended SWIR detector.

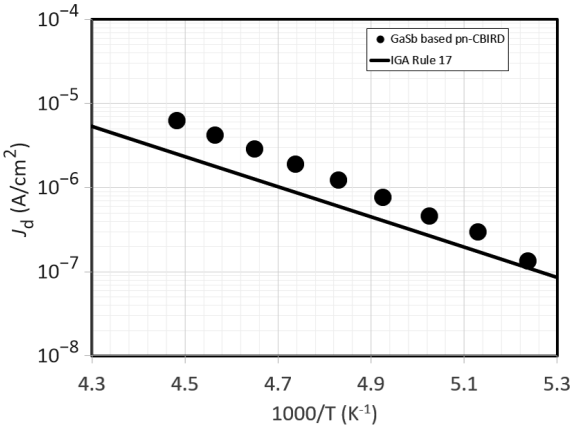


**Fig. 11.** Arrhenius plot of the dark current density measurement at various temperatures from 200 K to 300 K and −50 mV bias for the GaSb-based pn-CBIRD extended SWIR detector.

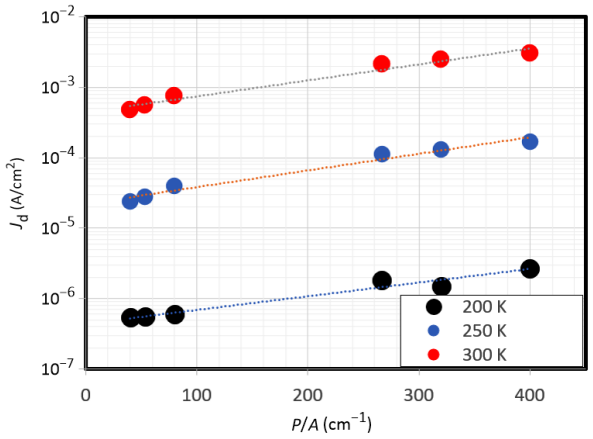


**Fig. 12.** Perimeter over area analysis of the pn-CBIRD dark current density at 200 K, 250 K and 300 K. Strong perimeter dependence is observed, indicating a significant mesa surface contribution to the dark current density.

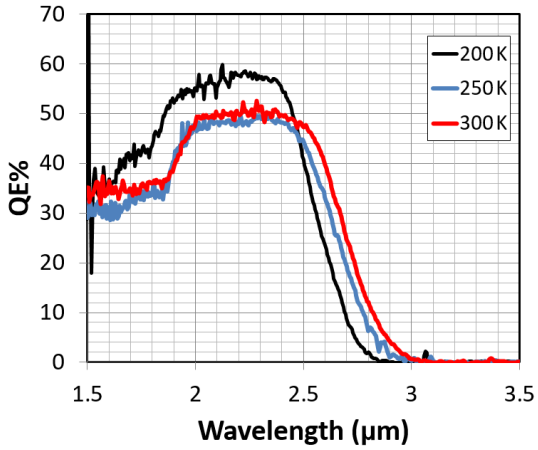


**Fig. 13.** External QE of the GaSb based pn-CBIRD extended SWIR detector measured at various temperatures from 200 K to 300 K.

shifts to about 2.7 μm by 300 K. The QE magnitude is stable over the temperature range from < 200 K, although by 300 K it has decreased substantially from near 60% to 40%, but remains high in comparison to the current state-of-the-art in InGaAs/GaAsSb based superlattice approach.

In Fig. 14, the magnitude of the QE at 2 μm measurement wavelength, over the lower temperature range from 80 K to 200 K, is shown for the pn-CBIRD device overlaid with corresponding data taken from an InGaAsSb nBp device grown and processed by IntelliEPI as a reference structure. The nBp device has both a similar bandgap and a similar structure to the pn-CBIRD, while having n-doping throughout the 4 um thick absorber. The nBp device, which is based on a fully n-type absorber material, shows a strong temperature dependence, while the pn-CBIRD structure shows a fixed QE magnitude. The indication is that, with the n-type InGaAsSb material, the diffusion length is substantially less than the 4 μm absorber thickness. The p-type material uses the much higher mobility electron as the minority carrier, resulting in increased diffusion length, but the p-type material is affected by the presence of surface pn junctions which tend to introduce tunnelling dark current, especially at higher bias. The combination of n-type and p-type absorber

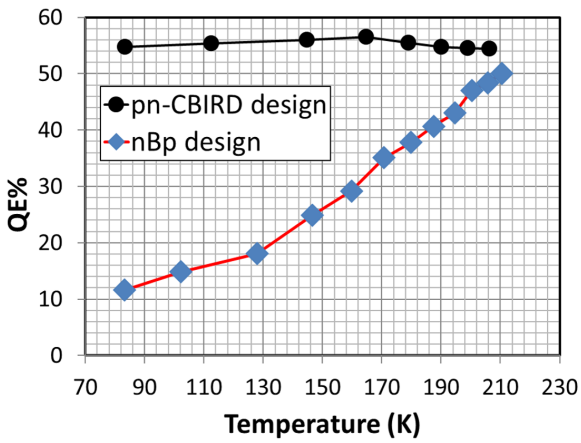


**Fig. 14.** External QE of the GaSb-based pn-CBIRD extended SWIR detector measured at various temperatures from 80 K to 200 K compared with nBp detector structure.

material retains the full responsivity benefit of the 4 um thick absorber but allows for a shallower mesa etch depth, reducing exposed p-type surface. The pn-CBIRD is able to circumvent the reduction in diffusion length by limiting the thickness of the n-region to 2 μm and utilizing 2 μm of p-type absorber. With operating temperatures above ~200 K, the QE of both devices converge as the hole diffusion length becomes > 4 μm. For most applications, device operation will occur above 200 K, allowing either device architecture to be applicable. The pn-CBIRD is best applied in devices which require low temperature, < 200 K, operation such as dual-spectrum devices where the sister band limits operating temperature.

### *3.3. Comparsion of the InP-based and GaSb-based detectivity*

In order to directly compare the device performance of the two approaches, the detectivity at the various operating temperatures are shown overlaid in Fig. 15. The GaSb approach is advantaged both in terms of extended cut-off wavelength and the magnitude of the detectivity in the spectral region where both structures are sensitive. While there is performance advantage of the GaSb approach, the InP solution remains attractive due to the potential for seamless adoption into InP-based SWIR platforms and industry.

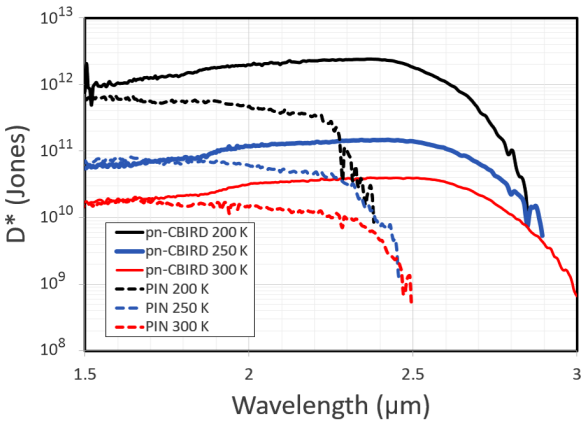


**Fig. 15.** Zero-degree field of view detectivity comparison for the InP-base InGaAs/GaAsSb PIN and the GaSb-based pn-CBIRD extended SWIR detector test devices.

## 4. Conclusions

The authors report two approaches based on III-V production MBE to address detection in the extended SWIR spectral band. The first approach is based on growth of lattice matched InGaAs/GaAsSb superlattice on InP substrate with tunable bandgap in the 2–3 um range. The InP-based approach takes advantage of the commercial InP-based processing infrastructure for device and array fabrication. The second approach leverages GaSb-based FPA manufacturing and is based on bulk random alloy InGaAsSb, which is tunable from 1.7 µm to 4.5 µm and lattice matched to the GaSb lattice constant. The authors have assessed the performance of these materials relative to commercially available extended SWIR devices through comparison to IGA Rule 17 dark current performance level. The materials compare favourably to commercial technology and present additional options to address the challenging extended SWIR spectral band.

## Acknowledgements

Our Sb-MBE growth and GaSb wafer manufacturing capabilities were established with support from DoD, particularly from FAST-FPA, VISTA, MANTECH and SBIR/STTR programs. In particular, the authors would like to thank the Night Vision and Electronic Sensors Directorate: M. Tidrow, S. Bandara, L. Aitchison, L. Zheng, and N. Supola; Jet Propulsion Laboratory: D. Ting, A. Soibel, C. Hill, L. Hoglund, and S. Gunpala; Naval Research Laboratory: E. Aifer, C.L. Canedy, I. Vurgaftman, J.A. Nolde, C.A. Affouda, and J.R. Meyer. The authors would also acknowledge the staff at Intelligent Epitaxy Technology, Inc. (IntelliEPI) for their support with epi material growth and characterization.

## References

[1] Jain, M. *et al*. Development of an ultrahigh-performance infrared detector platform for advanced spectroscopic sensing systems. *Proc. SPIE* **9073**, 18–25 (2014). https://doi.org/10.1117/12.2054328

[2] Kim, M. S. *et al*. Visible to SWIR hyperspectral imaging for produce safety and quality evaluation. *Sens. Instrum. Food Qual. Saf.* **5**, 155–164 (2011). https://doi.org/10.1007/s11694-012-9122-3

[3] Shaikh, M. S., Jaferzadeh, K. & Thörnberg, B. Extending effective dynamic range of hyperspectral line cameras for short wave infrared imaging. *Sensors* **22**, 1817 (2022). https://doi.org/10.3390/s22051817

[4] Wooten, M. Superluminescent Diodes at 2.4 Microns from GaInAsSb/AlGaAsSb Quantum Well Heterostructures for Optical Glucose Sensing. (The University of Iowa, 2013).

[5] Martyniuk, P., Antoszewski, J., Martyniuk, M., Faraone, L. & Rogalski, A. New concepts in infrared photodetector designs. *Appl. Phys. Rev*. **1**, 041102 (2014). https://doi.org/10.1063/1.4896193

[6] Ji, X. *et al*. Deep-level traps induced dark currents in extended wavelength InxGa1−xAs/InP photodetector. *J. Appl. Phys*. **114**, 224502 (2013). https://doi.org/10.1063/1.4838041

[7] Dehzangi, A. *et al*. Type–II superlattices base visible/extended short–wavelength infrared photodetectors with a bandstructure–engineered photo–generated carrier extractor. *Sci. Rep*. **9**, 503 (2019). https://doi.org/10.1038/s41598-019-41494-6

[8] Uliel, Y. *et al*. Type-II superlattice based photodiodes for short wave infrared detection. *Infrared Phys. Technol*. **84**, 63–71 (2017). https://doi.org/10.1016/j.infrared.2017.02.003

[9] Craig, A. P. *et al*. Short-wave infrared barriode detectors using InGaAsSb absorption material lattice matched to GaSb. *Appl. Phys. Lett*. **106**, 201103 (2015). https://doi.org/10.1063/1.4921468

[10] Lumb, M. P. *et al.* Drift-diffusion modeling of InP-based triple junction solar cells. *Proc. SPIE* **8620**, 86201G (2013). https://doi.org/10.1117/12.2005332

[11] Zhang, Y. G. *et al*. IGA-rule 17 for performance estimation of wavelength-extended InGaAs photodetectors: validity and limitations. *Appl. Opt*. **57**, D141–D144 (2018). https://doi.org/10.1364/AO.57.00D141

[12] Ting, D. Z. *et al*. Long wavelength InAs/InAsSb superlattice barrier infrared detectors with p-type absorber quantum efficiency enhancement. *Appl. Phys. Lett*. **118**, 133503 (2021). https://doi.org/10.1063/5.0047937

[13] Ting, D. Z. Development of type-II superlattice long wavelength infrared focal plane arrays for land imaging. *Infrared Phys. Technol*. **123**, 10413 (2022). https://doi.org/10.1016/j.infrared.2022.104133